infrastructures

MDPI

Article

Experimental Study of Bending and Torsional Effects in Walking-Induced Infrastructure Vibrations: The Pasternak Footbridge

Ghita Eslami Varzaneh, Elisa Bassoli, Federico Ponsi and Loris Vincenzi *

Department of Engineering "Enzo Ferrari", University of Modena and Reggio Emilia, 41125 Modena, Italy; ghita.eslami@unimore.it (G.E.V.); elisa.bassoli@unimore.it (E.B.); federico.ponsi@unimore.it (F.P.)
* Correspondence: loris.vincenzi@unimore.it; Tel.: +39-059-205-6213

Abstract

Slender, lightweight and modern footbridges are particularly susceptible to vibrations induced by pedestrian activity. While extensive research has focused on vertical and lateral forces produced by walking, torsional moments generated by eccentrically walking pedestrians remain largely overlooked. Traditional assessments typically neglect these torsional effects, which can be critical when eccentric pedestrian loading excites torsional modes, especially in footbridges with asymmetric geometries. To address this, the paper considers the coupling between bending and torsional effects in both the pedestrian action and structure reaction, including pedestrian forces and moments, as well as bending-induced deflections and torsion-induced rotations of the cross-sections. A simplified method is also presented, allowing standard bending-only analyses to be easily adapted to include torsional effects using analytically derived correction factors. For validation, several experimental tests are conducted on an asymmetric curved footbridge located in Modena, Italy, characterised by coupled bending-torsional vertical modes and hosting different pedestrian densities, pacing frequencies, and crowd distributions (both uniform and eccentric). Experimental and numerical analyses demonstrate that neglecting torsional effects oversimplifies the assessment, highlighting the importance of accounting for bending-torsion coupling for the serviceability of asymmetric footbridges under eccentric near-resonance loading.

Keywords: footbridge serviceability assessment; pedestrian-induced vibrations; torsional effects; crowd loading; eccentricities; experimental validation

Academic Editors: Miao Su, Zhiping Zeng, Min Wu and Fuming Wang

Received: 23 December 2025
Revised: 16 January 2026
Accepted: 20 January 2026
Published: 21 January 2026

1. Introduction

Modern footbridges are particularly susceptible to human-induced excitation due to their slender and lightweight design, which results in low natural frequencies that may coincide with pedestrian walking frequencies [1,2]. This can produce near-resonance conditions, as experienced by the Millennium Bridge in London [3] and the Solférino footbridge in Paris [4], making vibration serviceability a critical aspect of footbridge design and assessment. As a result, the civil engineering community is actively advancing research in this area [5–8]. Pedestrians exert forces in three directions (horizontal-lateral, horizontal-longitudinal, and vertical), with the vertical component being the largest [9]. To assess vertical vibrations, serviceability checks have traditionally focused on structural bending modes, as these primarily govern the vertical response to pedestrian forces. This approach is reflected both in the research literature and in the few available design guidelines [10–13].

Nevertheless, highly asymmetric footbridges with striking visual impact are becoming increasingly common [14–20]. In such structures, the primary vertical modes may involve coupled bending-torsion or even pure torsion, rather than pure bending. When pedestrian loading excites these modes, torsion-related rotations of the structure might potentially amplify vertical structural responses beyond what is predicted by bending-only analyses, which only account for deflection. Eccentric walking or uneven crowd distributions may further enhance vertical vibrations, as torsional moments are generated in addition to the pedestrian vertical forces, making it essential to consider the interaction between translational and rotational effects when evaluating vibration serviceability. Neglecting these torsional contributions can lead to an underestimation of vertical vibrations, and consequently, to overly conservative design decisions [21]. Despite the increasing recognition of torsional dynamics in modern footbridge design, research on this topic remains limited, leaving a significant gap in the literature [22]. Indeed, serviceability-oriented experimental studies are rarely supported by numerical models incorporating human-induced torsion. This limitation affects not only simple straight footbridges [23,24] but also more complex geometries [25,26], such as curved or asymmetric layouts that exhibit bending-torsional modes within typical pedestrian pacing frequencies.

In this context, the paper addresses the coupling between bending and torsion in both pedestrian action (vertical forces and moments) and structural response (cross-sectional translations and rotations). The combined effects of bending and torsional vibrations are investigated through a comprehensive approach that includes experimental tests on a real structure, detailed numerical simulations, and a simplified methodology based on multiplication factors [21]. These factors allow to correct bending-only analyses to account for torsional effects, including (i) the potential amplification of vertical vibrations at the centre of mass and (ii) the shift of maximum vibrations away from the centre of mass due to rotational effects. Multiplication factors are derived analytically by comparing the equations of motion under bending-only and coupled bending-torsion scenarios, ensuring they are not influenced by numerical calibration errors. They only depend on modal parameters, structural and loading eccentricities. This allows their calculation a priori, to quantify the contribution of torsional effects in a given application case and determine whether detailed bending-torsion analyses are necessary.

First, to quantify the contribution of torsional behaviour to the overall structural vibrations, a parametric analysis of the multiplication factors is carried out, assessing the influence of both load and structural eccentricity. Subsequently, an experimental campaign is carried out on a highly asymmetric steel footbridge with a curved layout, a configuration that makes the structure particularly susceptible to coupled bending-torsional vibrations. The experimental results are compared with both detailed numerical simulations and predictions obtained using the multiplication factor-based approach. The tests consider several loading scenarios, including uniformly and non-uniformly distributed pedestrian crowds across the deck, as well as different pacing frequencies and crowd densities. The experimental validation demonstrates that all these aspects have a strong impact on the structural response, and highlights the importance of accounting for bending-torsion coupling in serviceability assessments of asymmetric footbridges under eccentric pedestrian loading. Lastly, further numerical analyses are carried out using the Latin Hypercube Sampling [27] and the Social Force Model [28,29] to assess the crowd-induced bending and torsional vibrations over a wider range of pedestrian traffic levels. Particular emphasis is given to the definition of an equivalent moment arm for crowd scenarios, which is required to establish the multiplication factors according to the presented simplified approach. In particular, the simulations examine whether the crowd can be assumed to be uniformly

distributed across the deck for the calculation of the equivalent moment arm, as such an assumption is necessary for a rapid multiplication factor-based assessment.

The paper is organized as follows. Section 2 introduces the traditional bending-only mathematical framework, presents its extension to include bending-torsion coupling, and analytically derives the corresponding multiplication factors. Section 3 presents a parametric analysis of the multiplication factors in relation to their governing parameters. Section 4 deals with the experimental tests conducted on the Pasternak footbridge. Section 5 describes the numerical analyses performed for the specific application cases. Section 6 discusses the experimental validation of the numerical predictions. Section 7 conducts further numerical analyses to investigate the crowd equivalent moment arm. Finally, Section 8 provides the conclusions.

2. Mathematical Modelling

This section deals with mathematical formulations, including the bending-only (Section 2.1) and bending-torsion (Section 2.2) frameworks, as well as their comparison, which leads to the definition of multiplication factors (Section 2.3). Please refer to [21] for further details.

2.1. Bending-Only Framework

The structural response to pedestrian loading is typically evaluated using the Euler–Bernoulli beam model, which represents the structure as a linear elastic beam. Under this assumption and considering only the vertical displacement degree-of-freedom w of the n discretised beam nodes (excluding torsional rotation and transverse deformation), the corresponding equation of motion is

$$\boldsymbol{M_w}\ddot{\boldsymbol{w}}(t) + \boldsymbol{C_w}\dot{\boldsymbol{w}}(t) + \boldsymbol{K_w}\boldsymbol{w}(t) = \boldsymbol{P_w}(t) \tag{1}$$

where $\boldsymbol{w}(t)$ is the n-by-1 vector containing nodal vertical displacements at time t; $\boldsymbol{M_w}$, $\boldsymbol{C_w}$ and $\boldsymbol{K_w}$ are the n-by-n mass, damping and stiffness matrices, respectively; $\boldsymbol{P_w}(t)$ is the n-by-1 pedestrian loading acting on the beam over time.

Expressing the structural behaviour as a sum of contributions from the beam natural modes of vibration (i.e., modal expansion) and exploiting the orthogonality of the mode shapes, the coupled system can be decoupled into a set of independent second-order ordinary differential equations, each associated with a single vibration mode. The resulting equations govern the modal coordinate $q_j(t)$ for each j-th mode:

$$\ddot{q}_j(t) + 2\xi_j\omega_j\dot{q}_j(t) + \omega_j^2 q_j(t) = \frac{P_j(t)}{M_j} \tag{2}$$

where mode j behaves as a single-degree-of-freedom system characterised by its circular frequency ω_j, damping ratio ξ_j, modal mass:

$$M_j = \boldsymbol{\phi_{w,j}}^{\mathrm{T}}\boldsymbol{M_w}\boldsymbol{\phi_{w,j}} \tag{3}$$

and generalised external force:

$$P_j(t) = \boldsymbol{\phi_{w,j}}^{\mathrm{T}}\boldsymbol{P_w}(t) \tag{4}$$

with $\boldsymbol{\phi_{w,j}}$ denoting the mode shape.

Once the modal coordinate $q_j(t)$ is computed, it is transformed back into modal displacement as

$$\boldsymbol{w_j}(t) = \boldsymbol{\phi_{w,j}}q_j(t) \tag{5}$$

Finally, the overall structural response is reconstructed via modal superposition, summing the contributions from all modes.

2.2. Bending-Torsion Framework

The coupled bending-torsion formulation considers that each of the n discretised beam nodes is characterised by both a vertical displacement due to bending w and a rotation due to torsion θ. The corresponding equation of motion for the dynamic system can be written in matrix form as

$$\begin{bmatrix} \boldsymbol{M}_w & \boldsymbol{M}_{w\theta} \\ \boldsymbol{M}_{\theta w} & \boldsymbol{M}_\theta \end{bmatrix} \begin{bmatrix} \ddot{\boldsymbol{w}}(t) \\ \ddot{\boldsymbol{\theta}}(t) \end{bmatrix} + \begin{bmatrix} \boldsymbol{C}_w & \boldsymbol{C}_{w\theta} \\ \boldsymbol{C}_{\theta w} & \boldsymbol{C}_\theta \end{bmatrix} \begin{bmatrix} \dot{\boldsymbol{w}}(t) \\ \dot{\boldsymbol{\theta}}(t) \end{bmatrix} + \begin{bmatrix} \boldsymbol{K}_w & \boldsymbol{K}_{w\theta} \\ \boldsymbol{K}_{\theta w} & \boldsymbol{K}_\theta \end{bmatrix} \begin{bmatrix} \boldsymbol{w}(t) \\ \boldsymbol{\theta}(t) \end{bmatrix} = \begin{bmatrix} \boldsymbol{P}_w(t) \\ \boldsymbol{P}_\theta(t) \end{bmatrix} \tag{6}$$

where $\boldsymbol{w}(t)$ and $\boldsymbol{\theta}(t)$ are n-by-1 vectors representing bending-related displacements and torsion-related rotations at the n nodes; in the mass, damping and stiffness matrices, the diagonal n-by-n blocks represent the pure bending ($\boldsymbol{M}_w$, $\boldsymbol{C}_w$, $\boldsymbol{K}_w$) or pure torsional ($\boldsymbol{M}_\theta$, $\boldsymbol{C}_\theta$, $\boldsymbol{K}_\theta$) contributions, while off-diagonal n-by-n blocks account for the coupling between vertical and torsional motion ($\boldsymbol{M}_{w\theta} = \boldsymbol{M}_{\theta w}$, $\boldsymbol{C}_{w\theta} = \boldsymbol{C}_{\theta w}$, $\boldsymbol{K}_{w\theta} = \boldsymbol{K}_{\theta w}$); $\boldsymbol{P}_w(t)$ and $\boldsymbol{P}_\theta(t)$ are the n-by-1 forces corresponding to displacement degrees of freedom and moments corresponding to rotation degrees of freedom. In this formulation, the human-induced moment $\boldsymbol{P}_\theta(t)$ can be obtained by multiplying the pedestrian force vector $\boldsymbol{P}_w(t)$ by the moment arm vector $\boldsymbol{d}_\theta(t)$, where each component of $\boldsymbol{d}_\theta$ represents the distance from the n-th nodal force application point to the corresponding cross-section centre of mass: $\boldsymbol{P}_\theta(t) = \mathrm{diag}(\boldsymbol{P}_w(t))\, \boldsymbol{d}_\theta$.

Note that the off-diagonal mass blocks vanish when the rotational degree of freedom θ at each node is defined about the cross-section centre of mass, as assumed here, leading to $\boldsymbol{M}_{w\theta} = \boldsymbol{M}_{\theta w} = 0$. In contrast, the off-diagonal damping and stiffness blocks, may be nonzero due to geometric asymmetry, which allows vertical bending to induce torsional rotation.

By applying modal decomposition and the orthogonality of mode shapes, the equation of motion is decoupled into components corresponding to each mode j. The system is thus reduced to independent single-degree-of-freedom equations, with each characterised by its own time-dependent modal amplitude $Q_j(t)$:

$$\ddot{Q}_j(t) + 2\xi_j \omega_j \dot{Q}_j(t) + \omega_j^2 Q_j(t) = \frac{P_j^*(t)}{M_j^*} \tag{7}$$

where the modal mass is obtained from the translational mass $\boldsymbol{M}_w$ and rotational mass $\boldsymbol{M}_\theta$, each weighted by the corresponding mode shape for displacements $\boldsymbol{\phi}_{w,j}$ and rotations $\boldsymbol{\phi}_{\theta,j}$, as

$$M_j^* = \boldsymbol{\phi}_{w,j}{}^{\mathrm{T}} \boldsymbol{M}_w \boldsymbol{\phi}_{w,j} + \boldsymbol{\phi}_{\theta,j}{}^{\mathrm{T}} \boldsymbol{M}_\theta \boldsymbol{\phi}_{\theta,j} \tag{8}$$

The modal generalised force is determined by projecting external forces $\boldsymbol{P}_w(t)$ and moments $\boldsymbol{P}_\theta(t)$ in modal basis:

$$P_j^*(t) = \boldsymbol{\phi}_{w,j}{}^{\mathrm{T}} \boldsymbol{P}_w(t) + \boldsymbol{\phi}_{\theta,j}{}^{\mathrm{T}} \left(\mathrm{diag}(\boldsymbol{P}_w(t))\, \boldsymbol{d}_\theta\right) \tag{9}$$

Once the modal amplitude $Q_j(t)$ is calculated, the modal displacements and rotations are obtained from the mode shapes:

$$\begin{bmatrix} \boldsymbol{w}_j(t) \\ \boldsymbol{\theta}_j(t) \end{bmatrix} = \begin{bmatrix} \boldsymbol{\phi}_{w,j} \\ \boldsymbol{\phi}_{\theta,j} \end{bmatrix} Q_j(t) \tag{10}$$

and can then be combined to compute the overall vertical displacement at a generic point H on the cross-section, located a distance e from the centre of mass:

$$\boldsymbol{W_{H,j}}(t) = \boldsymbol{w_j}(t) + \boldsymbol{\theta_j}(t)\boldsymbol{e} \tag{11}$$

Lastly, the total response combining all modes can be evaluated through modal superposition.

2.3. Multiplication Factors

To enable a quick and straightforward inclusion of torsional contributions to vertical vibrations, two multiplication factors are introduced. The first modifies the bending-related vertical acceleration at the cross-section centre of mass G to include torsional contributions, while the second scales this value to estimate the acceleration at any point H on the section, accounting for the growing influence of rotational effects with distance e from G. Accordingly, they are referred to as the torsional multiplication factor and the positional multiplication factor, as indicated by their respective subscripts.

The torsional multiplication factor α_{tors}, evaluated at a selected representative node i (e.g., at midspan), is obtained by comparing the modal displacement from the bending-only ($\boldsymbol{\phi_{w,j}} q_j$) and bending–torsion ($\boldsymbol{\phi_{w,j}} Q_j + \boldsymbol{\phi_{\theta,j}} Q_j$) formulations. With consistent mode normalisation (unit maximum vertical displacement and correspondingly scaled rotations) this is equivalent to comparing the modal forces, namely to evaluate the ratio of the right-hand side of Equations (7) and (2):

$$\alpha_{\text{tors}} = \left(1 + \frac{\phi_{\theta,ji}}{\phi_{w,ji}} d_\theta\right) \Big/ \left(1 + \frac{\boldsymbol{\phi_{\theta,j}}^{\mathrm{T}} \boldsymbol{M_\theta} \boldsymbol{\phi_{\theta,j}}}{\boldsymbol{\phi_{w,j}}^{\mathrm{T}} \boldsymbol{M_w} \boldsymbol{\phi_{w,j}}}\right) \tag{12}$$

with $\phi_{w,ji}$ and $\phi_{\theta,ji}$ being the i-th component of $\boldsymbol{\phi_{w,j}}$ and $\boldsymbol{\phi_{\theta,j}}$, respectively.

The torsional factor accounts for the effect of rotations at the cross-section mass centre G. Its sign and magnitude depend on the orientation of torsional rotations relative to bending deflections (mode shape ratio), on the location of the load d_θ, which can either counteract or enhance the rotational contribution, and on the relative rotational inertia (ratio of rotational to translational modal masses). Together, these factors determine whether torsional rotations increase or decrease the vertical response at G. As concerns the definition of d_θ in crowd conditions, numerical simulations are discussed in Section 6.

The positional factor $\alpha_{\text{pos}}(H)$ extends this effect from the centre of mass G to any point H on the cross-section, based on its distance e to G. It is derived from Equation (11) by comparing the structural response at a generic point H with eccentricity e, to that at the centre of mass G, where $e = 0$ and the rotational contribution vanishes. Taking the ratio of these two responses yields:

$$\alpha_{\text{pos}}(H) = 1 + \frac{\phi_{\theta,ji}}{\phi_{w,ji}} e \tag{13}$$

The magnitude and sign of the positional factor indicate whether rotations at H amplify or oppose the bending displacement.

3. Parametric Study of Multiplication Factors

To investigate the dependence of the multiplication factors on the governing parameters, a parametric analysis is conducted. The multiplication factors α_{tors} and $\alpha_{\text{pos}}(H)$ are evaluated at midspan and, for the sake of brevity, the quantities $\phi_{w,ji}$, and $\phi_{\theta,ji}$ are hereafter denoted as ϕ_w, and ϕ_θ, respectively. The analysis considers modal configurations ranging from predominantly first bending modes (with $\phi_w = 1$ and $\phi_\theta = 0$), to predominantly torsional modes (with $\phi_w = 0$ and $\phi_\theta = \pm 1$), as well as intermediate coupled

cases. Loading eccentricity d_θ and positional eccentricity e are both varied from -1.5 to 1.5 m considering a typical deck width of 3 m. The torsional multiplication factor α_{tors} is examined first. Referring to Equation (12), the contribution of the numerator is isolated by setting the denominator equal to unity. This is achieved by imposing $r = 0$, where r denotes the ratio between the rotational and translational generalised masses, namely $\boldsymbol{\phi}_{\theta,j}{}^{\mathrm{T}}\boldsymbol{M}_\theta\boldsymbol{\phi}_{\theta,j}/\boldsymbol{\phi}_{w,j}{}^{\mathrm{T}}\boldsymbol{M}_w\boldsymbol{\phi}_{w,j}$. The condition $r = 0$ therefore corresponds to a translational modal mass that is dominant with respect to the rotational one.

Under this assumption, the torsional multiplication factor is reported in Figure 1a. The results indicate a strong dependence of α_{tors} on the modal shape components evaluated at the considered cross-section, as well as on the loading moment arm d_θ. When $\phi_\theta = 0$, the bending-torsion formulation reduces to the bending-only case at G, yielding $\alpha_{\text{tors}} = 1$ independently of d_θ. For nonzero ϕ_θ, the sign and magnitude of α_{tors} are governed by the combined effect of ϕ_θ and d_θ. When these parameters have the same sign, the load eccentricity amplifies the rotational contribution, resulting in a positive α_{tors}. Conversely, when they have opposite signs, the eccentric loading opposes the torsional response, leading to a negative α_{tors}.

The contribution of the denominator is isolated in Figure 1b, imposing the numerator equal to unity through $d_\theta = 0$. In the absence of load eccentricity, the response at G obtained from the bending-only formulation coincides with that of the bending-torsional formulation, up to differences in the generalised modal mass. Therefore, in such instance, α_{tors} is a constant equal to $1/(1+r)$ (see Equation (12)).

Lastly, the parametric positional multiplication factor $\alpha_{\text{pos}}(H)$ is shown in Figure 1c, based on Equation (13). This factor equals unity when H coincides with G, i.e., when the positional eccentricity is $e = 0$. Otherwise, its value depends on whether point H is located in a region where rotational contributions amplify or counteract the pure translational deflection. This behaviour is governed by the relative sign of e and ϕ_θ, with same signs amplifying and opposite signs opposing.

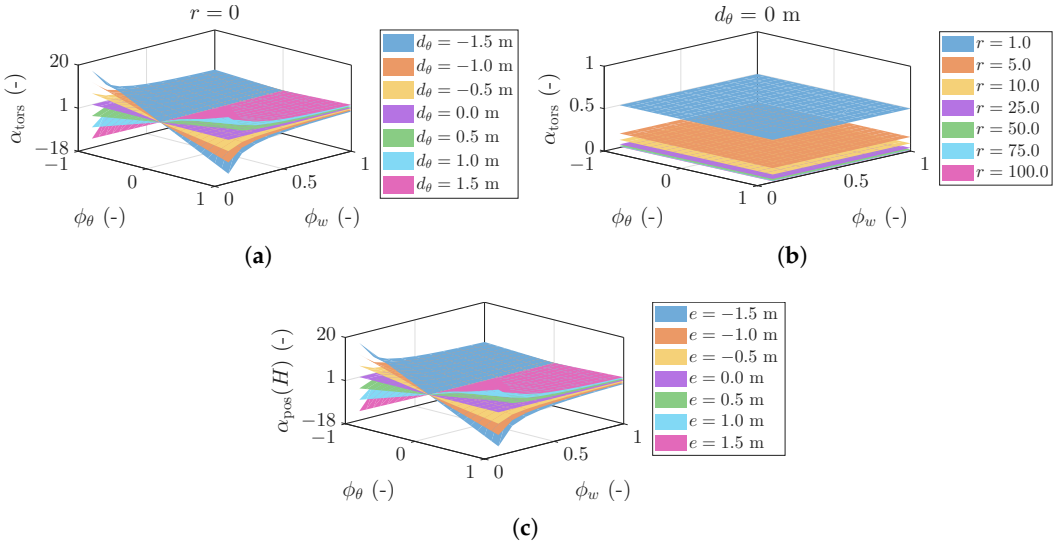

Figure 1. Multiplication factors: torsional factor with fixed (**a**) generalised modal mass ratio and (**b**) load eccentricity, (**c**) positional factor.

4. Experimental Results

This section presents the experimental results obtained on the Pasternak footbridge (Section 4.1). The tests included both measurements under ambient conditions for dynamic identification (Section 4.2) and with various pedestrian loading scenarios for serviceability assessment (Section 4.3).

4.1. Pasternak Footbridge

The Pasternak footbridge is a curved cable-stayed structure, completed in 2008, spanning approximately 170 m over a major freeway intersection in Modena, Italy. As illustrated in Figures 2 and 3, the bridge comprises a central curved span with a curvilinear length of 60 m and two 55 m long S-shaped access ramps. The main span is supported by cables connected to two V-shaped steel towers. Each tower consists of inclined towers interconnected by X-bracing. The towers are approximately 18 m high and inclined by about 15° from the vertical. The lateral access ramps are composed of multiple spans, supported by V-shaped precast concrete piers.

(**a**) (**b**)

Figure 2. Pasternak footbridge: structure layout from (**a**) south and (**b**) north sides.

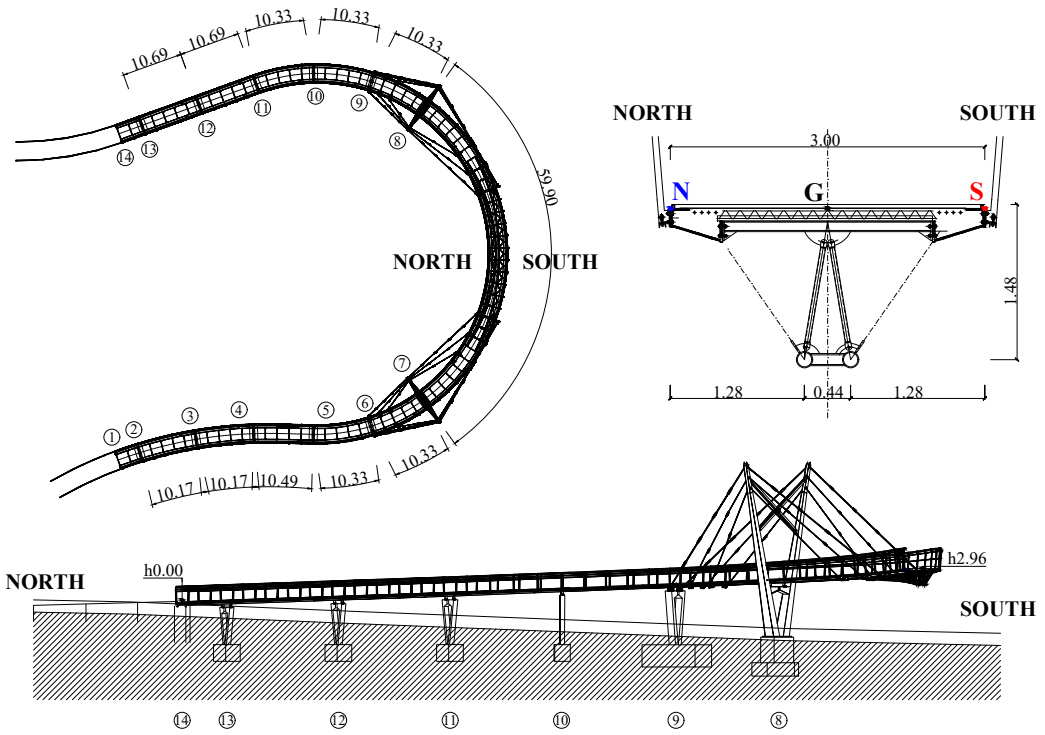

Figure 3. Pasternak footbridge: plan, half-elevation, and typical cross-section (all dimensions in metres). The span supports are numbered sequentially from 1 to 14, from west to east.

The central span has a constant width of 3 m and a uniform radius of approximately 32 m. The deck is made of steel beams supporting a concrete slab, while the main span includes a spatial truss girder formed by circular hollow steel profiles connected to the composite steel-concrete deck. The geometry of the girder varies along the length of the

main span, resulting in a different relative position between the hollow profiles and the deck at each cross-section. At the deck level, two longitudinal open-shaped concrete-filled chords are connected transversely with H- and L-shaped steel profiles. The towers are constructed from prismatic hollow sections with variable cross-sections, linked by H-shaped bracing using bolted connections. The bridge is equipped with steel parapets along its entire length.

4.2. Dynamic Identification

The dynamic analyses focused on the 60 m curved central span, where biaxial MEMS accelerometers were installed at approximately 4 m intervals. The sensors measured accelerations in the vertical and radial directions and were positioned on both sides of the deck (hereafter referred to as the north and south sides) to capture the torsional behaviour. Due to the limited number of available accelerometers, two measurement setups were implemented, with some sensors common to both configurations, allowing the combination of data from the different setups. Configurations are illustrated in Figure 4, in red and blue colours.

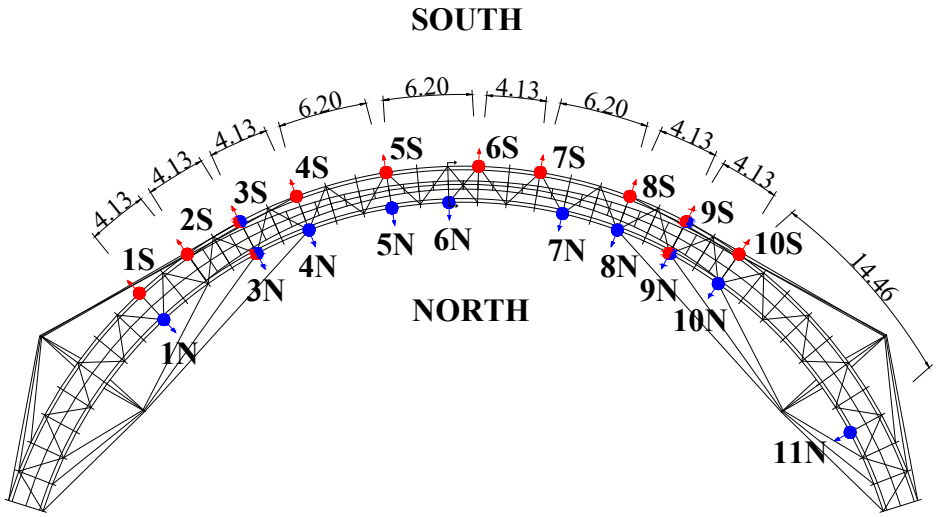

Figure 4. Pasternak footbridge: experimental layout with sensor IDs, locations, and mutual distances (in metres) for the two configurations, in red and blue.

Accelerations measured under ambient environmental conditions were used as input for OMA (Operational Modal Analysis) to identify the structural modal properties. Specifically, the EFDD (Enhanced Frequency Domain Decomposition) method [30,31] was applied. Following the PoSER (Post Separate Estimation Re-scaling) procedure [32], modal parameters were first estimated independently for each setup and then re-scaled and merged to obtain global mode shapes. Re-scaling was performed through a least-squares fitting of the reference sensor portions of each partial mode shape, ensuring consistency across the different measurement setups.

Modal parameters are illustrated in Figure 5, including vertical mode shapes at the deck edges (north and south sides indicated in blue and red, respectively), natural frequencies and damping ratios. Due to the complex geometry of the structure, as expected, all identified modes involve both bending and torsional components. Moreover, the footbridge is highly susceptible to pedestrian-induced excitation, since the natural frequencies of the first two modes (1.46 and 2.27 Hz) lie within the typical range of pedestrian pacing frequencies.

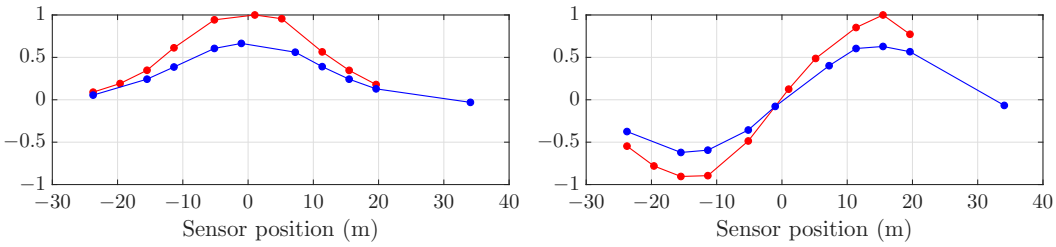

(**a**) Mode 1, $f_1 = 1.46$ Hz, $\xi_1 = 0.67$ %

(**b**) Mode 2, $f_2 = 2.27$ Hz, $\xi_2 = 0.56$ %

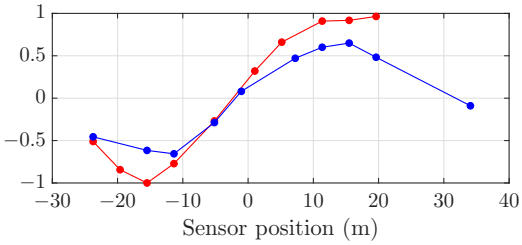

(**c**) Mode 3, $f_3 = 3.21$ Hz, $\xi_3 = 0.39$ %

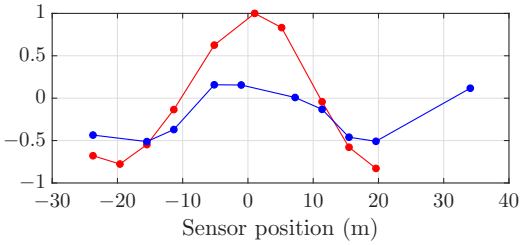

(**d**) Mode 4, $f_4 = 4.95$ Hz, $\xi_4 = 0.40$ %

Figure 5. Experimental tests: (**a**) first, (**b**) second, (**c**) third, and (**d**) fourth bending-torsional vertical modes. North inner edge in blue, south outer edge in red.

4.3. Pedestrian Excitation

To assess the footbridge response to pedestrian loading, a series of experimental tests was conducted. Pedestrian groups of varying sizes were instructed to walk across the bridge in a synchronised manner, at different step frequencies. To improve synchronisation among participants, a megaphone and a metronome were used to regulate the pace.

A group of 12 pedestrians was asked to walk in single file along the north side of the footbridge. Larger groups of 44 pedestrians were tested both: (i) while completely filling the deck and walking in a single, uniform direction, and (ii) moving in a closed loop between locations 7N and 4S (see Figure 4 for location IDs), with pedestrians in side files walking in opposite directions. The step frequencies and group sizes for the different tests are summarised in Table 1, with walking types illustrated in Figure 6.

Table 1. Experimental tests: pedestrian layouts.

Test ID	Step Frequency (Hz)	N_{ped} (-)	Walking Type
A	1.40	12	Single-file side
B	1.60	12	Single-file side
C	1.80	12	Single-file side
D	1.40	44	Distributed
E	1.40	44	Single-file loop

In Tests A, D, and E, the step frequency was set to 1.4 Hz to excite the footbridge first vertical mode, with a natural frequency of 1.46 Hz (symmetric mode with maximum amplitude at the midspan). Tests B and C were conducted to also assess the response under out-of-resonance conditions. Vertical accelerations recorded by the sensor closest to midspan (location 6N) during 1.4 Hz walking are depicted in Figure 7, with maximum absolute values $\ddot{W}_{exp}$ indicated by blue dots. The absolute peak accelerations $\ddot{W}_{exp}$ for all tests are reported in Table 2. The results show that near-resonance conditions (Tests A, D, E) lead to higher vibration levels than out-of-resonance cases (Tests B, C), regardless of crowd size (Test A involves the fewest pedestrians yet the largest vibrations). Indeed, the worst-case scenario does not necessarily correspond to the highest crowd density, but rather to a combination of crowd mass and the alignment of pacing and natural frequencies.

Moreover, for the same number of pedestrians and step frequency, eccentric walking (Test E) produces a larger response compared to distributed loading (Test D), underscoring the importance of explicitly accounting for human-induced moments in addition to forces.

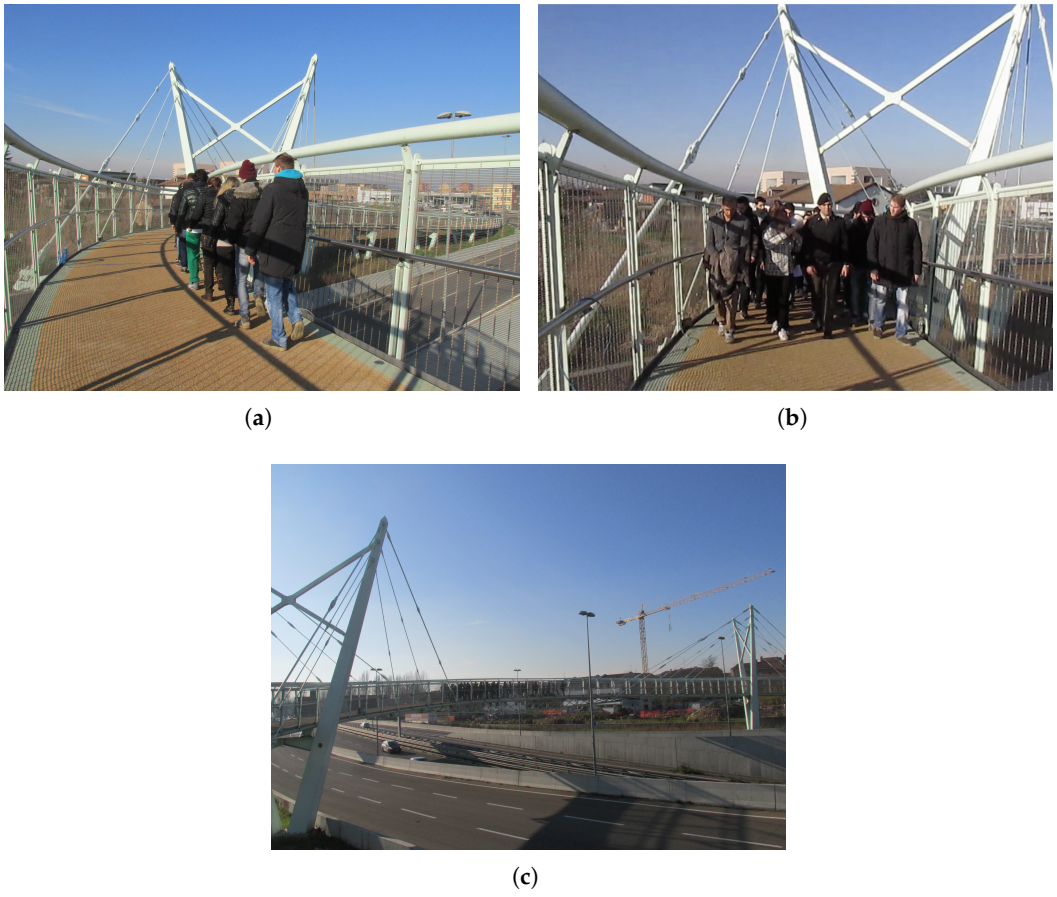

Figure 6. Experimental tests: (**a**) single-file side crossing, (**b**) distributed crossing, and (**c**) single-file loop walking.

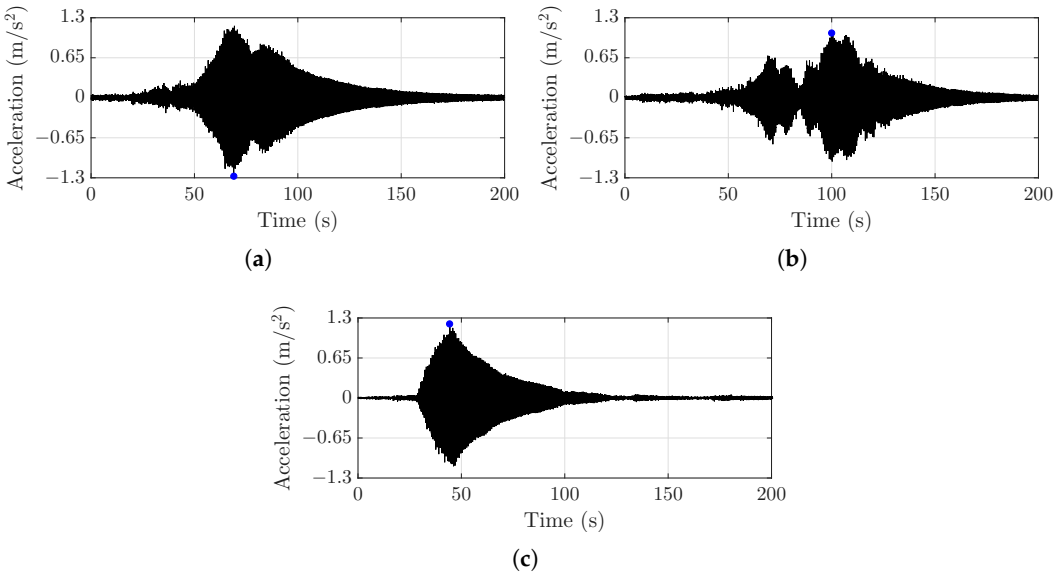

Figure 7. Experimental results: accelerations recorded at 6N during Test (**a**) A, (**b**) D and (**c**) E, with blue dots denoting the absolute peaks.

Table 2. Experimental results: peak accelerations $\ddot{W}_{exp}$ recorded at position 6N.

Test ID	Experimental Accelerations (m/s^2)
A	1.2739
B	0.5067
C	0.3256
D	1.0523
E	1.2035

5. Numerical Predictions

This section presents simulations to numerically predict the experimentally recorded accelerations. The step-by-step pedestrian load model introduced in Section 5.1 is adopted. The analyses are carried out using both the bending-only formulation, the coupled bending-torsion formulation, and the multiplication factor approach, as illustrated in Section 5.2, allowing a direct comparison of their predicted structural responses.

5.1. Pedestrian Loading

Regarding pedestrian loading, this paper adopts the single-step model proposed in [33], in which the z-th footfall force $P_z(t)$ is represented through a five-harmonic Fourier series:

$$P_z(t) = G_p \sum_{k=1}^{5} DLF_k \sin\left(\frac{\pi k}{T_c} t\right) \qquad 0 \le t \le T_c \tag{14}$$

In Equation (14), G_p (N) is the subject weight, here assumed as 73.85 kg, consistent with the population-average reported in [34]; k (-) is the harmonic counter; DLF_k (-) is the k-th dynamic load factor; T_c (s) is the foot-ground contact time. According to [33], step parameters are all dependent on the pacing frequency f_s (Hz), including the period $T = 1/f_s$ (s), the contact time $T_c = T/0.76$ (s), the overlapping time between left and right feet $\Delta t = 0.24T_c$ (s), and the dynamic load factors DLF_k (please refer to [33] for the specific formulations).

In this paper, the pacing frequency f_s is set as indicated in Table 1 depending on the specific test, and all the step parameters are computed accordingly. After defining the individual step force $P_z(t)$, the periodic walking time history is obtained by replicating at T time increments and l_s space increments. Here, l_s denotes the step length, which is set to 0.71 m as the statistical average observed in [35]. Each step force is thus linked to a specific time and position along the span. For example, $P_z(t)$ is shown spatially at a representative cross-section in Figure 8. Its repetition at intervals T produces the time-varying force shown in Figure 9a, generated by a representative pedestrian walking at 1.4 Hz.

Once the pedestrian loading is computed, crowd conditions are generated by replicating it N_{ped} times, where N_{ped} is the number of pedestrians, at intervals of $2T$. The latter is chosen to maintain sufficient spacing between consecutive pedestrians, ensuring a realistic representation of the loading. Specifically, for single-file walking (either crossing the footbridge or along a loop), $2T$ is applied between all pedestrians, whereas for distributed walking, $2T$ corresponds to the shift between groups of four side-by-side pedestrians, as four parallel lines were formed during the tests (please see Figure 6b).

To obtain the modal force for the bending-only framework (i.e., $P_j(t)$) each step force $P_z(t)$ is weighted by the amplitude of the translational mode shape $\boldsymbol{\phi}_{w,j}$ evaluated at the corresponding footfall location, i.e., interpolated at l_s increments. Regarding the generalised modal force for the bending-torsion framework (i.e., $P_j^*(t)$), each step force $P_z(t)$ contributes both through the translational mode component $\boldsymbol{\phi}_{w,j}$ and, scaled by the corresponding step moment arm $\boldsymbol{d}_\theta$, through the rotational mode component $\boldsymbol{\phi}_{\theta,j}$. This

allows accounting for both the step force and the moment it induces when the force is eccentric by d_θ with respect to G, as illustrated in the example of Figure 8.

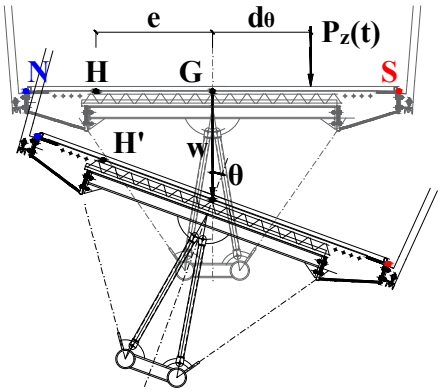

Figure 8. Numerical analyses: displacement w and rotational θ degrees of freedom, whose combination yields the overall vertical displacement of a generic point H located at a distance e from the centre of mass G, for example as induced by a footfall force $P_z(t)$ with eccentricity d_θ. Both d_θ and e are referenced to G, with positive values towards the south edge S.

The cross-sectional coordinate is centred at the centre of mass G, located on the centreline, with positive values toward the south side (S) and negative values toward the north side (N). Therefore, $\boldsymbol{d_\theta}$ is set to -1.5 m for pedestrians walking in single file on the north side of the deck. When pedestrians change direction while walking in a loop, the sign of $\boldsymbol{d_\theta}$ is reversed, and the mode shapes $\boldsymbol{\phi_{w,j}}$ and $\boldsymbol{\phi_{\theta,j}}$ are mirrored accordingly. Please note that the path followed during loop walking is asymmetric relative to the midspan. Lastly, for cases in which the deck is fully occupied, the moment arm $\boldsymbol{d_\theta}$ is assigned values of -1.5, -0.5, 0.5, and 1.5 m to the four parallel lines of pedestrians, in order to reflect the actual distribution of the crowd.

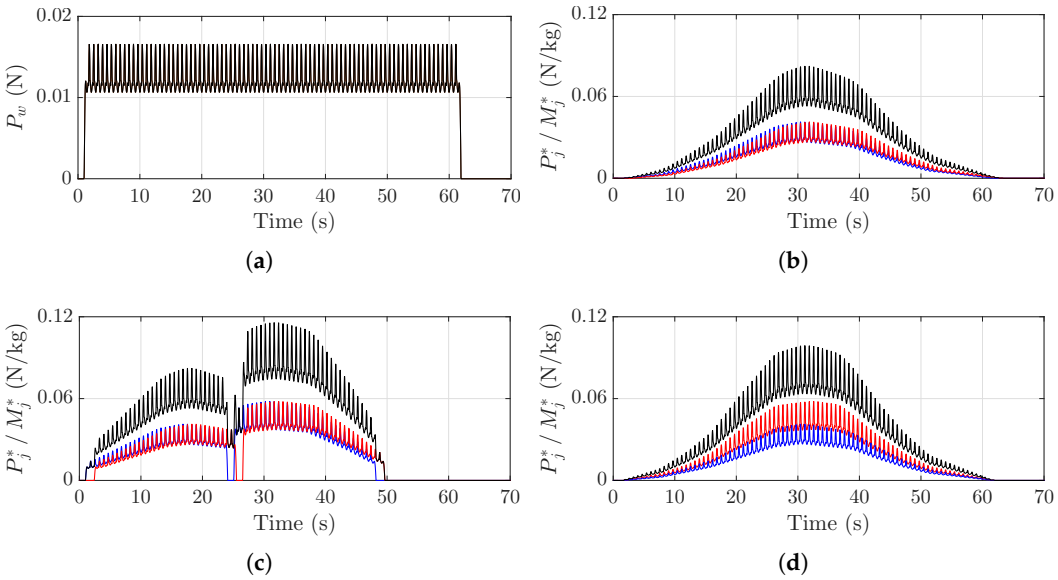

Figure 9. Numerical analyses: (**a**) step-by-step force from an example pedestrian; overall generalised modal force (in black) from two example pedestrians (in blue and red, respectively) walking: (**b**) in a single file, (**c**) along a loop, (**d**) distributively.

Figure 9b–d illustrates the generalised modal force for the tested layouts, showing two pedestrians (blue and red) as a representative example. In Figure 9b, the contributions of the two pedestrians are identical but time-shifted, as they walk one behind the other

in a single file with the same eccentricity. A similar behaviour is observed in Figure 9c, with a change in amplitude due to the direction reversal in loop walking, which suddenly alters the sign of the moment arm. By contrast, in Figure 9d, the contributions of the two pedestrians differ in amplitude as they walk side by side under distributed loading, with different moment arms generating different moment components in their generalised modal forces.

5.2. Structural Responses

To numerically evaluate the serviceability of the experimentally tested footbridge, as is common in the literature, the structural response is calculated considering the contribution of a single mode. Specifically, the first mode ($j = 1$) is considered, as the most excited by pedestrian activity across all the tested pacing frequencies.

Although the girder exhibits slight asymmetry along the length of the main span, the centre of mass G is assumed to coincide with the centreline at each cross-section for the sake of simplicity.

To evaluate the translational mode shape $\boldsymbol{\phi}_{w,j}$ at the centre of mass G, the experimental components obtained at the north and south edges of the deck are averaged. For the determination of the rotational mode shape $\boldsymbol{\phi}_{\theta,j}$, the angle between the two experimentally measured vertical components at the edges is calculated. Finally, $\boldsymbol{\phi}_{w,j}$ is normalised to unit, and $\boldsymbol{\phi}_{\theta,j}$ is scaled accordingly.

The total mass of 250,000 kg is scaled linearly with the main span length and lumped at nodes spaced at 1 m intervals. The translational mass matrix $\boldsymbol{M}_w$ is evaluated consistently. As concerns the rotational mass matrix $\boldsymbol{M}_\theta$, the polar moment of inertia is computed by distributing the nodal mass over the section and summing the contributions of each discretised area relative to the section centroid.

Bending-only and bending-torsion frameworks are implemented as outlined in Sections 2.1 and 2.2, respectively, to evaluate the maximum absolute accelerations where experimental data are available. In the bending-only formulation, the assumption of rigid deflection implies identical peak accelerations at G and N, i.e., $\ddot{w}_{G,1} = \ddot{w}_{N,1}$. In contrast, the bending-torsional framework accounts for the rotational contribution at any generic point H on the cross-section, depending on its distance e from G, through Equation (11). Similarly to d_θ, e is measured from G and assigned positive values towards S, where translational and rotational contributions are additive (see the example in Figure 8). Since the experimental acceleration at the midspan is recorded at location 6N, $H = N$ is here selected, yielding peak responses $\ddot{W}_{N,1}$. Maximum absolute accelerations predicted by the two frameworks are listed in the first two columns of Table 3.

As concerns the simplified approach, multiplication factors are computed based on Equations (12) and (13). For cases with pedestrians walking in single files along the north side of the deck, the equivalent moment arm is $d_\theta = -1.5$ m, resulting in a torsional multiplication factor of $\alpha_{\text{tors}} = 0.8265$. In scenarios with looped or stream walking, the equivalent moment arm is $d_\theta = 0$ m, as pedestrians on opposite sides of the deck counterbalance each other, leading to $\alpha_{\text{tors}} = 0.9876$. The positional multiplication factor $\alpha_{\text{pos}}(N) = 0.8369$ is calculated at the deck edge N, where $e = -1.5$ m.

Bending-only results are scaled by the torsional and positional multiplication factors, to respectively account for torsional rotation at the centre of mass and rotational effects at the deck north side. The resulting estimates $\ddot{w}_{G,1}\alpha_{\text{tors}}\alpha_{\text{pos}}(N)$ are reported in the last column of Table 3. The two torsion-aware methods (detailed bending-torsion framework and simplified approach) produce estimates in close agreement, both diverging from the traditional bending-only model. The following section discusses an in-depth comparison and interpretation of the results, validated against experiments.

Table 3. Numerical results: peak acceleration computed at position 6N, including the bending-only $\ddot{w}_{G,1}$, bending-torsion $\ddot{W}_{N,1}$, and simplified $\ddot{w}_{G,1}\alpha_{tors}\alpha_{pos}(N)$ estimations.

Test ID	Bending-Only acc. (m/s^2)	Bending-Torsion acc. (m/s^2)	Simplified Method acc. (m/s^2)
A	1.9656	1.3320	1.3596
B	0.7541	0.5134	0.5216
C	0.5029	0.3425	0.3479
D	1.3431	1.1102	1.1101
E	1.4524	1.2419	1.2004

6. Experimental Validation

This section addresses the discussion of the results, comparing the experimental structural responses with those predicted numerically.

First, it is important to note that, regardless of the modelling framework, the numerical results (see Table 3) are higher than the experimental ones (see Table 2). This can be explained by the fact that, despite measures taken to ensure synchronisation, the pedestrians were likely not perfectly synchronised during the tests.

Furthermore, bending-only simulations yield higher structural responses compared to bending-torsion simulations. This occurs because, on the north side of the deck (where experimental data is available), rotations act against the deflections, whereas on the south side, rotations amplify the deflections (please refer to the schematic in Figure 8). Therefore, bending-only simulations are not over-conservative in an absolute sense, but they tend to overestimate the structural response at one extremity (north N) and underestimate it at the other (south S).

Following these clarifications, Table 4 reports the relative errors between the experimental and numerical accelerations, defined as:

$$\delta_{\ddot{W}} = \frac{|\ddot{W}_{exp} - \ddot{W}_{num}|}{\ddot{W}_{exp}} 100 \tag{15}$$

where $\ddot{W}_{exp}$ denotes the experimental response recorded at location 6N, listed in Table 2, and $\ddot{W}_{num}$ refers to the numerical predictions yielded by the various approaches adopted. Specifically, $\ddot{W}_{num}$ indicates $\ddot{w}_{G,1}$, $\ddot{W}_{N,1}$, and $\ddot{w}_{G,1}\alpha_{tors}\alpha_{pos}(N)$ for the bending-only, bending-torsion, and simplified approaches, respectively, corresponding to the first, second, and third columns of Table 3.

In Tests A, B, and C, with eccentric single-file walking, the bending-torsion framework yields consistently lower errors compared to the bending-only framework, with average errors of 4% and 53%, respectively. In Tests D (distributed crossing) and E (loop walking), the pedestrian loading is more balanced across the deck, resulting in smaller error differences between the two models. Nevertheless, the bending-torsion framework still exhibits an order-of-magnitude lower error.

Table 4. Comparison of experimental and numerical results: relative errors $\delta_{\ddot{W}}$.

Test ID	Bending-Only Error (%)	Bending-Torsion Error (%)	Simplified Method Error (%)
A	54.30	4.56	6.73
B	48.83	1.32	2.94
C	54.45	5.19	6.84
D	27.63	5.50	5.49
E	20.68	3.19	0.25

Table 4 also confirms the efficiency of the simplified approach, which performs a traditional bending-only computation and incorporates torsional effects through two multiplication factors. The method yields very low errors despite its simplicity, remaining on the order of 5% across all tested scenarios. The accuracy is essentially equivalent to that of the detailed bending-torsion framework, yet the method preserves the simplicity needed during design or assessment stages.

7. Crowd Equivalent Moment Arm

This section deals with the moment arm definition in real-world crowd scenarios, as detailed in the following.

To implement the simplified approach, the multiplication factors can be easily derived by only knowing the modal parameters, the eccentricity of the loading and that of cross-sectional edges. In the experimentally tested scenarios, the definition of the loading eccentricity is straightforward, as pedestrians were instructed to maintain predefined path. In real-world conditions, crowds are generally expected to be uniformly distributed across the deck, resulting in an equivalent moment arm d_θ for the torsional multiplication factor equal to the distance between the centreline (the crowd centre of mass) and the cross-sectional centre of mass.

To validate this hypothesis, statistical analyses are performed as described in the following. Latin Hypercube Sampling (LHS) [27] is used to generate representative pedestrian positions on the deck, offering a more uniform, space-filling distribution than purely random sampling. Monte Carlo analyses are performed with 10,000 simulations for each crowd density, ranging from 0.2 to 1.5 ped/m^2. For the 60 $\times$ 3 m^2 main span deck, this corresponds to simulate a number of points (i.e., pedestrians) ranging from 36 to 270. An example simulation is illustrated in Figure 10a, with blue and red colours indicating people walking on the north and south sides of the centreline.

The simulated points in the original X–Y coordinate system (please see Figure 10a) are mapped into a curvilinear x–y coordinate system, where the x-axis follows the curved trajectory of the central span and the y-axis represents the deck width. To simplify the simulation, the curved trajectory is then unwrapped into a linear configuration, taking advantage of the relatively small curvature of the central span. Note that, unlike the other numerical simulations performed, the reference system for the y coordinates is here centred at edge N rather than at G. In this way, the transverse positions of pedestrians range from 0 to 3 m, corresponding to the deck width.

For each simulation, the crowd centre of mass $\bar{y}$ is calculated by averaging the transverse coordinates y of all pedestrians. The mean and standard deviation of the crowd centre of mass are then computed across the 10,000 simulations for each density, where a location at 1.5 m corresponds to the centreline (see Figure 10b).

For each simulation, the relative difference between the simulated crowd centre of mass $\bar{y}$ and $y_0 = 1.5$ m (the value under the uniform distribution assumption, corresponding to $d_\theta = 0$ m) is determined as

$$\delta_y = \frac{\bar{y} - y_0}{y_0} 100 \tag{16}$$

The mean and standard deviation of δ_y across all simulations are shown in Figure 10c. Notably, the average difference decreases with increasing density, as denser crowds more closely approximate a uniform distribution. The standard deviation of δ_y is also small, even at low densities, confirming that the uniformity assumption provides a reliable and computationally efficient basis for simplified analyses.

However, a clarification is needed. While crowds are on average uniformly distributed, instantaneous off-centre arrangements can occur, generating rotations that amplify vertical

vibrations. Thus, the equivalent lever arm accurately predicts mean accelerations, but may underestimate peak values, as peak accelerations are more likely to occur when instantaneous eccentricities arise.

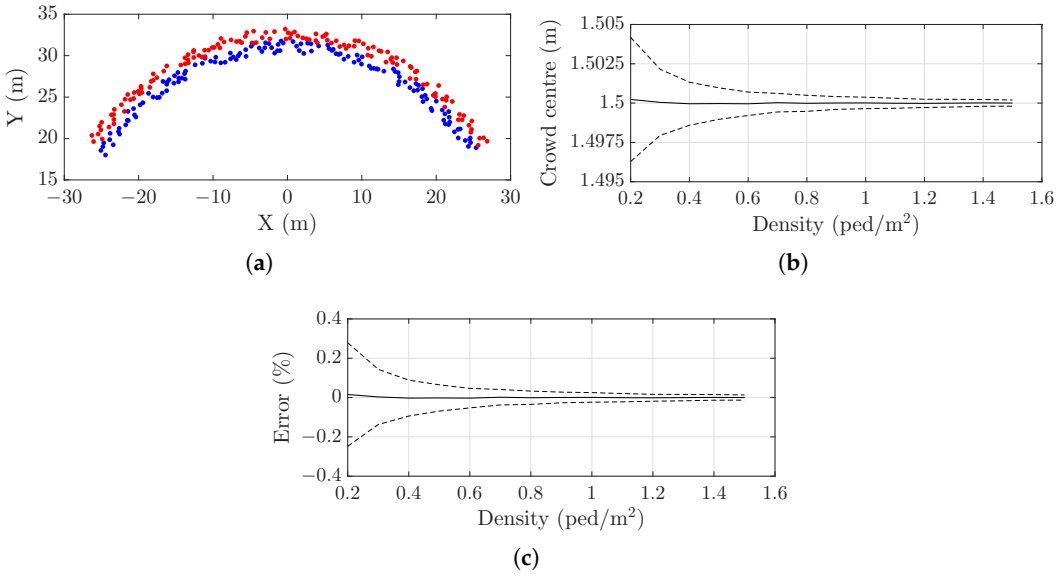

Figure 10. Latin Hypercube Sampling analyses: (**a**) example simulation with 1.5 ped/m^2, with blue and red dots representing pedestrians on the north and south halves of the deck, respectively; (**b**) crowd centre of mass $\bar{y}$ as a function of crowd density; (**c**) error δ_y in considering a uniform crowd distribution versus traffic density. In (**b**,**c**), solid lines represent mean values, dashed lines indicate the confidence interval corresponding to one standard deviation.

To confirm this, further numerical analyses are carried out, modelling crowd motion through the Social Force Model (SFM) [28]. The latter captures pedestrian dynamics while explicitly incorporating individual heterogeneity, environmental effects, and human-human interactions. Specifically, the SFM version introduced in [29] is implemented, calibrated such that the average crowd velocity decreases with increasing crowd density, as observed in [36]. Inter-pedestrian variability is introduced by randomly assigning body mass and preferred walking speed according to the distributions in [34,37], while deviations from the target pace arise from boundary avoidance and local interactions with neighbouring pedestrians.

For each examined crowd density, 100 simulations are performed. Density is kept constant by returning pedestrians who have completed crossing to the span start. The SFM provides time histories of pedestrian positions and velocities, from which instantaneous step frequencies are obtained using the cubic speed-frequency relationship reported in [38]. For each pedestrian, footfall times are determined iteratively, with each step occurring after a time interval equal to the inverse of the step frequency evaluated at the previous footfall, and footfall locations are extracted from the time-varying pedestrian position at those times.

In the bending-only formulation, each footfall is modelled as a vertical walking force computed using the step-by-step loading approach of Equation (14). When bending-torsion coupling is included, a torsional moment is additionally applied, evaluated as the product of the step force and the lateral offset of the footfall position from the section centre of mass. In the simplified approach, multiplication factors turn: $\alpha_{\text{tors}} = 0.9876$ assuming $d_\theta = 0$ m, $\alpha_{\text{pos}}(N) = 0.8369$, $\alpha_{\text{pos}}(S) = 1.1581$.

Peak midspan accelerations due to SFM crowds are reported in Figure 11, including those obtained by the bending-only, bending-torsion, and simplified approaches. Specif-

ically, results are presented as the mean (solid line) and one standard deviation (dashed lines) over the 100 simulations performed for each crowd density, as functions of the traffic level and transverse coordinate e. Here, $e = -1.5$ m denotes the north side N (in blue), $e = 1.5$ m indicates the south side S (in red), and $e = 0$ m the centre of mass G (in black).

In the bending-torsion framework, the response varies along the cross-section, with higher accelerations where torsional-related rotation reinforces the bending-driven deflection (deck edge S) and lower accelerations where it opposes deflection (deck edge N). In the bending-only framework, the section undergoes rigid-body translation without any rotational component, producing identical responses at the deck edges N (in blue) and S (in red), and at the centre of mass G (in black). In the simplified approach, multiplication factors applied to bending-only responses effectively reproduce the acceleration variability along the transverse coordinate e.

Figure 12 shows the differences between the bending-torsion and the other two methods. As evident in Figure 12a, the bending-only system shows notable differences of approximately 40%. In Figure 12b, the simplified approach demonstrates consistently lower differences, around 10%. These are not driven by the positional amplification factor $\alpha_{\text{pos}}(H)$ (with $H = S$ or $H = N$), whose definition is free from uncertainty and thus produces negligible errors. In contrast, the torsional amplification factor α_{tors} depends on the crowd equivalent moment arm definition. The latter is here set to zero under the assumption of a uniformly distributed crowd, as confirmed by the LHS simulations. This condition holds in a time-averaged sense rather than instantaneously, which leads to expected deviations in peak estimates. Nevertheless, these deviations remain limited, and the simplified method can be considered satisfactorily validated, given the necessary assumptions for rapid assessments.

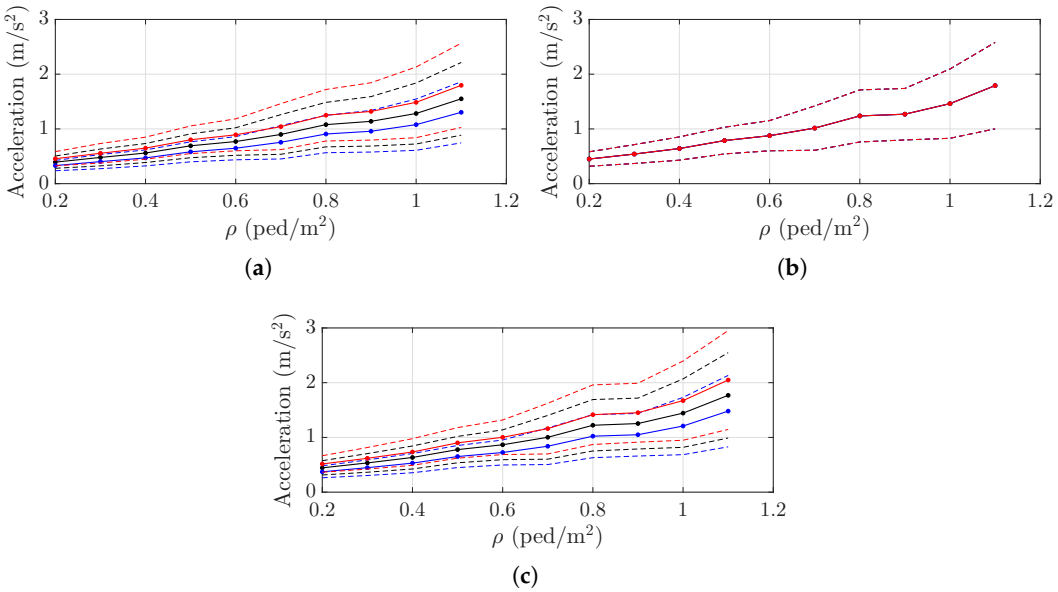

Figure 11. Social Force Model analyses: midspan peak accelerations at the deck edges N (in blue) and S (in red), and at the centre of mass G (in black) resulting from the (**a**) bending-torsion, (**b**) bending-only, and (**c**) multiplication-factor-based methods. The average and one standard deviation interval are marked in solid and dashed lines, respectively.

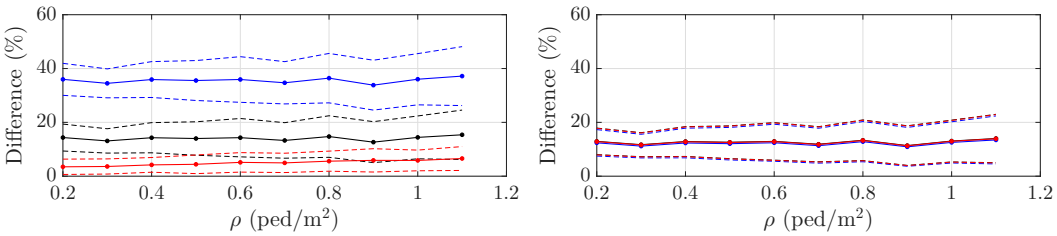

Figure 12. Social Force Model analyses: comparison of midspan peak accelerations at the deck edges *N* (in blue) and *S* (in red), and at the centre of mass *G* (in black) resulting from the (**a**) bending-torsion and bending-only frameworks, and (**b**) bending-torsion and multiplication-factor-based frameworks. The average and one standard deviation interval are marked in solid and dashed lines, respectively.

8. Conclusions

This paper addresses torsional effects induced by pedestrian activity. While bending-only analyses are well established, the inclusion of cross-sectional rotational degrees of freedom and the pedestrian-induced moment resulting from eccentric walking becomes necessary when the main torsional modes are excited, especially when structural geometries and loading are asymmetric. A detailed bending-torsion framework is presented, along with a simplified, rapid approach based on correction multiplication factors.

The performance of these methods is assessed through experimental tests conducted on a full-scale curved footbridge in Modena, Italy. The tested scenarios include both eccentric and uniform crowd distributions. Experimental results demonstrate that neglecting torsional effects can lead to substantial inaccuracies under real-world conditions, particularly for eccentric loading, with errors of up to approximately 50%. Both the detailed bending-torsion framework and the simplified method yield limited errors (around 5%), an order of magnitude smaller than those observed in conventional bending-only analyses.

The simplified approach allows the use of the traditional bending-only framework while correcting predictions with multiplication factors that account for torsional effects, thereby preserving the practicality and efficiency of the assessments. These factors are derived analytically, eliminating calibration uncertainties, and can be computed solely from the modal parameters, structural geometry, and loading eccentricity.

Regarding pedestrian loading eccentricity, the equivalent moment arm of the crowd is required. Numerical analyses using Latin Hypercube Sampling are conducted to assess realistic crowd configurations as a function of crowd density. Results confirm that assuming a uniform crowd distribution, with its centre of mass along the structural centreline, is a valid approximation, especially for dense crowds. However, peak accelerations are likely to occur under instantaneous eccentric configurations.

To investigate maximum structural responses induced by realistic crowd scenarios, the Social Force Model is adopted, accounting for inter-pedestrian variability, human-human interaction, and intra-personal variability driven by environmental influences. These simulations demonstrate that the assumption of crowd distribution uniformity leads to limited errors, confirming that the simplified approach provides sufficiently accurate estimates for practical assessments.

In conclusion, this study demonstrates that bending-only analyses are oversimplified and that accounting for torsional effects induced by pedestrian activity is essential, especially when pacing excites torsional modes or loading is eccentric, as confirmed experimentally. The mathematical frameworks adopted here do not consider cross-sectional transverse deformations or human-structure interaction, as in current guidelines, but they are torsion-aware, thus advancing the footbridge serviceability state-of-the-art.

Author Contributions: Conceptualization, G.E.V., F.P., E.B. and L.V.; methodology, G.E.V., E.B. and F.P.; formal analysis, G.E.V.; data curation, G.E.V. and E.B.; writing—original draft preparation, G.E.V.; writing—review and editing, F.P., E.B. and L.V.; supervision, L.V. All authors have read and agreed to the published version of the manuscript.

Funding: This research received no external funding.

Informed Consent Statement: Informed consent was obtained from all subjects involved.

Data Availability Statement: Data are available from the corresponding author on reasonable request.

Conflicts of Interest: The authors declare no conflicts of interest.

References

1. Zivanovic, S.; Pavic, A.; Reynolds, P. Vibration serviceability of footbridges under human-induced excitation: A literature review. *J. Sound Vib.* **2005**, *279*, 1–74. [CrossRef]
2. Racic, V.; Pavic, A.; Brownjohn, J.M.W. Experimental identification and analytical modelling of human walking forces: Literature review. *J. Sound Vib.* **2009**, *326*, 1–49. [CrossRef]
3. Dallard, P.; Fitzpatrick, T.; Flint, A.; Low, A.; Smith, R.; Willford, M.; Roche, M. London Millennium bridge: Pedestrian-induced lateral vibration. *J. Bridge Eng.* **2001**, *6*, 412–417. [CrossRef]
4. Dziuba, P.; Grillaud, G.; Flamand, O.; Sanquier, S.; Tétard, Y. La passerelle Solférino comportement dynamique (dynamic behaviour of the Solférino bridge). *Bull. Ouvrages Mét.* **2001**, *1*, 34–57.
5. Van Hauwermeiren, J.; Van Nimmen, K.; Van den Broeck, P.; Vergauwen, M. Vision-based methodology for characterizing the flow of a high-density crowd on footbridges: Strategy and application. *Infrastructures* **2020**, *5*, 51. [CrossRef]
6. Nicoletti, V.; Quarchioni, S.; Tentella, L.; Martini, R.; Gara, F. Experimental tests and numerical analyses for the dynamic characterization of a steel and wooden cable-stayed footbridge. *Infrastructures* **2023**, *8*, 100. [CrossRef]
7. Caloni, A.; Morfino, M.; Civera, M.; Surace, C. Structure-to-human interaction (H2SI): Pedestrian response to oscillating footbridges and considerations on their structural control and health monitoring. *Infrastructures* **2025**, *10*, 9. [CrossRef]
8. Zhao, C.; Jiang, Y.; Wang, J. A Computer vision-based pedestrian flow management system for footbridges and its applications. *Infrastructures* **2025**, *10*, 247. [CrossRef]
9. Bachmann, H.; Ammann, W. *Vibrations in Structures: Induced by Man and Machines*; International Association for Bridge and Structural Engineering: Zurich, Switzerland, 1987.
10. SETRA. *Footbridges—Assessment of Vibrational Behaviour of Footbridges Under Pedestrian Loading*; Technical Department for Transport, Roads and Bridges Engineering and Road Safety, Ministry of Transport and Infrastructure: Paris, France, 2006.
11. *ISO 10137*; Bases for Design of Structures—Serviceability of Buildings and Walkways Against Vibrations. International Organization for Standardization: Geneva, Switzerland, 2007.
12. BSI. *UK National Annex to Eurocode 1: Actions on Structures—Part 2: Traffic Loads on Bridges*; (NA to BS EN 1991-2:2003); British Standards Institution: London, UK, 2008.
13. HIVOSS. *Human Induced Vibrations of Steel Structures*; European Research program RFCS—Research Fund for Coal and Steel: Brussels, Belgium, 2008.
14. Caetano, E.; Cunha, A.; Magalhães, F.; Moutinho, C. Studies for controlling human-induced vibration of the Pedro e Inês footbridge, Portugal. Part 1: Assessment of dynamic behaviour. *Eng. Struct.* **2010**, *32*, 1069–1081. [CrossRef]
15. Roda-Casanova, V.; Hernández-Figueirido, D.; Sancho Bru, J.L.; Martínez-Rodrigo, M.D. Numerical modelling and vibration serviceability assessment of a steel footbridge with a significant 3D dynamic behaviour. *Proc. Inst. Mech. Eng. Part C J. Mech. Eng. Sci.* **2014**, *238*, 708–723. [CrossRef]
16. Bursi, O.S.; Kumar, A.; Abbiati, G.; Ceravolo, R. Identification, model updating, and validation of a steel twin deck curved cable-stayed footbridge. *Comput.-Aided Civ. Infrastruct. Eng.* **2014**, *29*, 703–722. [CrossRef]
17. Fenu, L.; Congiu, E.; Lavorato, D.; Briseghella, B.; Marano, G.C. Curved footbridges supported by a shell obtained through thrust network analysis. *J. Traffic Transp. Eng. (Engl. Ed.)* **2019**, *6*, 65–75. [CrossRef]
18. Miyachi, K.; Nakamura, S. Cable-stayed bridge with s-curved girder: Shake hands bridge. *Struct. Eng. Int.* **2021**, *31*, 504–515. [CrossRef]
19. Al-Smadi, Y.M.; Al-Rousan, R.Z.; Laradhi, A.A.; Avci, O. Vibration serviceability investigation of a curved footbridge. *Pract. Period. Struct. Des. Constr.* **2022**, *27*, 04022040. [CrossRef]
20. He, L.; Castoro, C.; Aloisio, A.; Zhang, Z.; Marano, G.C.; Gregori, A.; Deng, C.; Briseghella, B. Dynamic assessment, FE modelling and parametric updating of a butterfly- arch stress-ribbon pedestrian bridge. *Struct. Infrastruct. Eng.* **2022**, *18*, 1064–1075. [CrossRef]

21. Eslami Varzaneh, G.; Bassoli, E.; Vincenzi, L.; Aloisio, A.; Briseghella, B.; Tomasi, R. A novel framework for assessing the serviceability of footbridges under human-induced bending and torsional vibrations: From detailed formulation to simplified design method. *Struct. Infrastruct. Eng.* **2026**, 1–18. [CrossRef]
22. Bruno, L.; Venuti, F.; Nascé, V. Pedestrian-induced torsional vibrations of suspended footbridges: Proposal and evaluation of vibration countermeasures. *Eng. Struct.* **2012**, *36*, 228–238. [CrossRef]
23. Brownjohn, J.M.W.; Fok, P.; Roche, M.; Omenzetter, P. Long span steel pedestrian bridge at Singapore Changi Airport - Part 2: Crowd loading tests and vibration mitigation measures. *Struct. Eng.* **2004**, *82*, 28–34.
24. Van Nimmen, K.; Van Hauwermeiren, J.; Van den Broeck, P. Eeklo footbridge: Benchmark dataset on pedestrian-induced vibrations. *J. Bridge Eng.* **2021**, *26*, 1–17. [CrossRef]
25. Zhang, Y.; He, W.; Zhang, J.; Dong, H. Experimental and numerical investigation on dynamic properties and human-induced vibrations of an asymmetric steel-plated stress-ribbon footbridge. *Adv. Civ. Eng.* **2021**, *2021*, 2028378. [CrossRef]
26. Chen, X.; Geng, X.; Fu, W.; Tan, L.; Guan, J.; Liu, T. Vibration serviceability assessment of ribbon-shaped large-span footbridge at high altitudes under wind-pedestrians coupling effects. *Structures* **2024**, *66*, 106885. [CrossRef]
27. McKay, M.D.; Beckman, R.J.; Conover, W.J. A comparison of three methods for selecting values of input variables in the analysis of output from a computer code. *Technometrics* **1979**, *21*, 239–245. [PubMed]
28. Helbing, D.; Molnar, P. Social force model for pedestrian dynamics. *Phys. Rev. E* **1995**, *51*, 4282–4286. [CrossRef]
29. Bassoli, E.; Vincenzi, L. Parameter calibration of a social force model for the crowd-induced vibrations of footbridges. *Front. Built Environ.* **2021**, *7*, 656799. [CrossRef]
30. Brincker, R.; Zhang, L.; Andersen, P. Modal identification of output-only systems using frequency domain decomposition. *Smart Mater. Struct.* **2001**, *10*, 441. [CrossRef]
31. Brinker, R.; Ventura, C.; Andersen, P. Damping estimation by frequency domain decomposition. In *Proceedings of IMAC 19: A Conference on Structural Dynamics*; Society for Experimental Mechanics: Kissimmee, FL, USA, 2001.
32. Edwins, D.J. *Modal Testing: Theory, Practice and Application*; John Wiley & Sons: Hoboken, NJ, USA, 2007.
33. Li, Q.; Fan, J.; Nie, J.; Li, Q.; Chen, Y. Crowd-induced random vibration of footbridge and vibration control using multiple tuned mass dampers. *J. Sound Vib.* **2010**, *329*, 4068–4092. [CrossRef]
34. Portier, K.; Tolson, J.K.; Roberts, S.M. Body weight distributions for risk assessment. *Risk Anal.* **2007**, *27*, 11–26. [CrossRef]
35. Zivanovic, S.; Pavic, A.; Reynolds, P. Probability-based prediction of multi-mode vibration response to walking excitation. *Eng. Struct.* **2007**, *29*, 942–954. [CrossRef]
36. Weidmann, U. Transporttechnik der fußgänger: Transporttechnische eigenschaften des fußgängerverkehrs (literaturauswertung). *IVT Schriftenr.* **1993**, *90*, 1–84.
37. Buchmüller, S.; Weidmann, U. *Parameters of Pedestrians, Pedestrian Traffic and Walking Facilities*; Institut für Verkehrsplanung und Transportsysteme (IVT): Zurich, Switzerland, 2006.
38. Bruno, L.; Venuti, F. The pedestrian speed-density relation: Modelling and application. In *Proceedings of the 3rd International Conference on Footbridges*; Faculdade de Engenharia, Universidade do Porto (FEUP): Porto, Portugal, 2008.